BABEŞ-BOLYAI UNIVERSITY
CLUJ-NAPOCA
FACULTY OF PHYSICS

TRANSPORT PHENOMENA THROUGH COMPLEX MOLECULAR SYSTEMS

PhD. Thesis

PhD. Student: Radu-Bogdan Isai
Scientific Advisor prof. dr. Vasile Chiş

2014

Acknowledgments

First of all, I would like to thank the Lord, for all His help so far! I would also like to thank Him for the wonderful people He surrounded me.

I would like to thank my parents for their love and all their support. I'm also indebted to my brother and to Valentina.

I would like to thank prof. Vasile Chiş for accepting me for the doctoral studies, and also for his great support. He allowed me to understand more profoundly the DFT machinery.

I would also like to thank dr. Cristian Morari for introducing me to the DFT and NEGF, and his support throughout my Master and doctoral studies.

I would also like to thank prof. Stefano Sanvito for accepting me to have a internship in his group; I think it was a nice turning point for my thesis and also for my career.

I thank all members of the thesis jury for the consideration of accepting to judge my work and for giving me valuable insights on the topic.

I would like to give some special thanks to our IT engineer, Mrs. Teodora, for her moral and technical support during my research work.

I'm grateful to dr. Ivan Runnger and dr. Andrea Drogetti for sharing their friendship and their knowledge during my stay in Dublin. I have also enjoyed the collegiality of Amaury Melo Souza, Thomas Archer, Maria Stamenova, Meilin Bai, Sandip Bhattacharya.

I would like to thank to dr. Eugen Sorbalo for his friendship and his support - he is the main responsible for the last chapter for both my Master and doctoral theses!

I would not like to forget and thank Diana Bogdan, Radu Brătfălean, Daniel Bîlc, Alexandra Fălămaş, Cătălin and Ioana Ivaşcu, Nicoleta Mircescu, George Mile, Alex Okos, Gabriela Mocanu, Laci. I would like to give special thank to Sorina Garabagiu.

I would like to thank Mircea Oltean for taking care of my codes, compiling and recompiling them, until they work. I would also like to thank Călin Floare for his technical support at ITIM.

I'm profoundly indebted to Vlad T. and his family, Gicu S., Eugen M., Ilie M., Alexandru M., Anca R and her parents, Alin and Mariana, Samuel and Oana, Alex and Adela, Paula, Miha, Cătălin Ş., Cristi G., Claudia I., Beni T., Ruben T., Criti M. I could not forget the *Irish team*: Ica, Sorin, Patricia and Denis, Costel and Mia (and their parrents) and Nathan, Mugurel D., Dan, Nelu D.

I would also like to give special thanks to Bianca B, Olimpia C., Adela M, Aurora B., and last but not least Dana M.

I would like to remember also *my* students for giving me only the right quantity of distraction from computational problems! ... and I must confess, I enjoyed and I thank them for their company!

Computational resources have been provided by the Trinity Centre for High Performance Computing (Trinity College, Dublin) and by National Institute for Research and

Development of Isotopic and Molecular Technologies (Cluj-Napoca).

Financial support is acknowledged through the Sectorial Operational Programme for Human Resources Development 2007-2013, co-financed by the European Social Fund, under the project number POSDRU/107/1.5/S/76841.

Contents

Keywords: Density Functional Theory (DFT), Spin Crossover, Silicon Nanotubes, Scanning Tunneling Microscopy (STM), adsorption, vibrational properties, quantum transport.

Chapter 1

Introduction

The advent of the scanning tunnelling microscope (STM) in the 1980's gave important insights into the molecular world[1]. New fields, like molecular electronics, emerge and flourish due to the series of fundamental issues it poses and which have been receiving sound answers only recently. The main difference between transport through molecules/low dimensional systems and standard metals or semiconductors arise from Fermi surface collapse into a single or small number of energy levels (the highest occupied molecular orbital (HOMO) and the lowest unoccupied molecular orbital (LUMO))[2]. In addition, the nature and the line-up of these levels with the Fermi energy of the voltage probes determine most of the transport properties.

The most important aspect of transport phenomena through organic molecules is their potential use in spintronic devices, bringing memory and logic functionalities on the same chip. This is mainly due to the fact that the weak spin-orbit and hyperfine interactions in organic molecular materials preserves spin-coherence over times and distances much longer than in conventional metals or semiconductors, making those molecules ideal candidates for spintronic devices [3].

In this thesis, some of the most important aspects in *building* a molecular device are *probed*: the properties of the interconnections *material* - ideally a nanotube, the influence of the coupling strength on switching properties, and the influence of the more subtle van der Waals interaction on molecular structure and the molecular properties.

In the first chapter, the theoretical methods used for these investigations are presented, including the density functional theory, and an introduction to the non-equilibrium Green functions. In the end of this chapter, two implementations using both the DFT and NEGF methods, are compared on a test bed - the dehydrogenated aniline sandwiched between two (110) copper contacts.

In the second chapter, the electronic and vibrational properties of the Silicon nanotubes are discussed, based on their corresponding density of states. We also address the changes in the vibrational properties due to isotopic substitutions.

In the third chapter, we study the prototypical spin crossover molecule properties

(more precisely we focus on its electronic structure and the geometric distortion - as a preadsorption study) and its adsorption of on different substrates. The electronic properties of the adsorbed molecule are then discussed.

The role of dispersion corrected functionals on the structural and vibrational properties of the double decked Lutetium based phthalocyanine is discussed in the forth chapter.

We conclude our findings in the last chapter.

Chapter 2

Silicon nanotubes

2.1 Experimental and theoretical background

Probably one of the most representative system between all the nanostructures is the carbon nanotube. Although only recently rediscovered by Iijima[4], it attracted (and still attracts) much attention due to its physical and chemical properties. Unfortunately, its bottom-up integration in useful real-life devices is very difficult. In this chapter, we focus on a close *relative* of the carbon nanotube, which may ease the integration of nanostructures in feasible devices - the Silicon-based nanotube (SiNT)[5].

Although Silicon nanowires are more easier to be produced (and a lot of their properties are well known since 1960s[6]), studies on SiNT are scarce. Different structural models were proposed for these novel SiNTs (a good review can be found in Ref. [7]). Recently, Bai *et al.* [8] proposed geometric structures for square, pentagonal and hexagonal single-walled silicon nanotubes (Fig. 2.1). These structures maintain the fourfold coordination of silicon, but at different angles compared to the tetrahedral structure of cubic diamond silicon. Using *ab initio* calculations, Bai *et al.* argue that such structures have a zero band gap.

2.2 Computational details

We use the SIESTA package [9, 10] for the DFT calculations. To describe the electronic structure of the $3s$ electrons, we employed a double-ζ polarized basis set, while for the $3p$ electrons we used a triple-ζ polarized basis set. The energy shift used to build the basis set was 150 meV. We use Troullier-Martins norm conserving pseudopotentials [11] and the GGA (PBE version) [12] as exchange-correlation functional. In order to represent the grid related quantities we used an energy grid of 250 Ry. We relaxed the preliminary geometry of the system (i.e. atomic positions and cell length) by using the conjugate gradient method. The final gradients in the system were less than 10^{-3} eV/Å, while the

Model	d_0 [Å]	a_0 [Å]	N
5SiNT	2.43	2.44 (2.39)	19
6SiNT	2.42	2.44 (2.40)	23

Table 2.1: Geometric parameters of the SiNTs investigated in this work: d_0 denotes the interatomic distance for the atoms located in the same plane of the nanotube; a_0 represents the interplanar distance, while N is the number of layers used to build the supercells (see also Fig. 2.1). The values in parentheses indicate the results of Bai *et al.* [8].

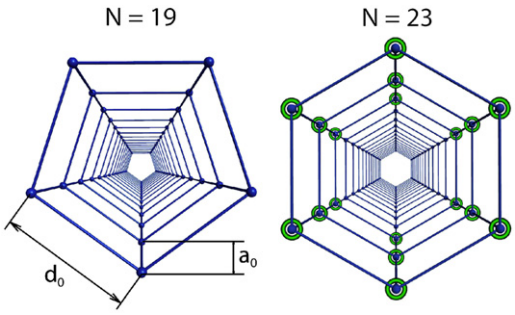

Figure 2.1: A 3D perspective representation of the geometric structures for 5SiNT and 6SiNT. We indicate the relevant geometric parameters. As an intuitive example, for 6SiNT we indicate by green circles the isotopic substitutions for three layers of the nanotube.

stress components were less than 5×10^{-6} eV/Å^3. The vibrational analysis was performed by using the frozen-phonons technique, as implemented in SIESTA.

We built the starting geometric structures for pentagonal (5SiNT) and hexagonal (6SiNT) silicon single-walled nanotubes starting from the results of Bai *et al.* [8] and using the supercell periodic approach for our study. The supercell geometry was taken to be tetragonal, with the dimension $L \times L \times L_z$, where the $\hat{z}$ direction is defined as the axial direction of the nanotubes with $L = 25$Å; L_z is 46.4Å (5SiNT) and 56.2Å (6SiNT). These values are obtained after a full relaxation of the atomic positions and of the cell length. The frozen-phonon technique requires carefully chosen size of the supercell used in calculation. Too short supercell can lead to wrong results; precisely, the resulting vibrational bands have negative frequencies. By gradually increasing the supercell in the $\hat{z}$ direction we found that, for the 5SiNT, a number of 19 layers produces converged results with no negative phononic bands. In the case of 6SiNT, we get converged results for a number of 23 layers.

The quality of the pseudopotentials used in our calculations was checked by comparing the results obtained for models systems ($Si_{25}H_{10}$ and $Si_{30}H_{12}$) with all-electrons calculation performed with Gaussian [13]. The same GGA functional (PBE) was used

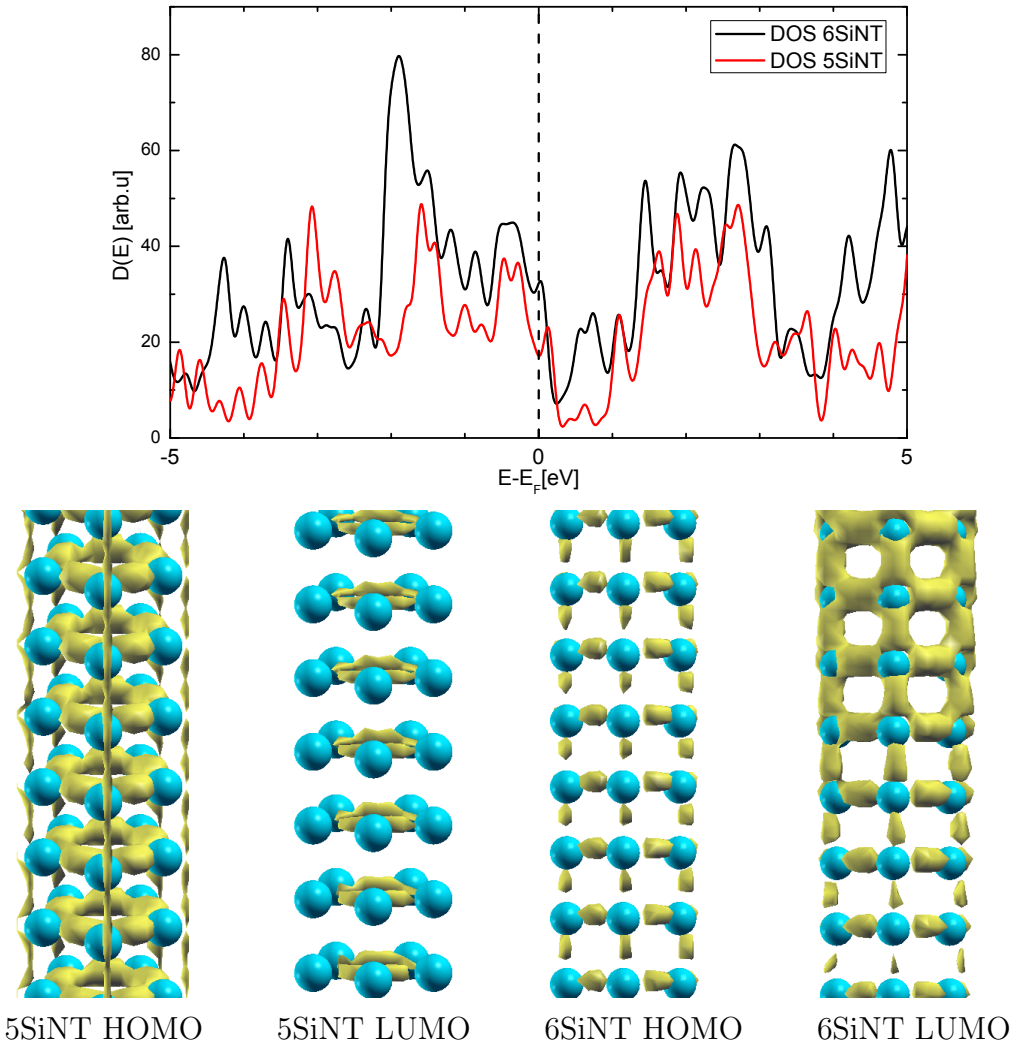

Figure 2.2: The electronic densities of states of the two types of SiNTs considered (top) and the LDOS of the frontier orbitals for the two species. Both species, show a non-zero density of states near the Fermi energy, followed by energy gaps. The widest gap occurs in the case of the 5 fold SiNT.

for all-electrons and pseudopotential calculations; a 6-31G(d) basis set was used for all-electron calculations. The overall geometry and most important the vibrational density of states give simillar results.

2.3 Electronic properties

Charge transport properties are mostly influenced by the electronic density of states near the Fermi level. To get an insight into the intrinsec electrical properties of the SiNTs the density of states for both species and the localized density of states (LDOS) for the frontier orbitals are presented in this section.

The electronic density of states (shown in Fig. 2.2) is not empty at the Fermi level, which suggest a good electrical conductivity of both SiNT species. Nevertheless, above

the Fermi energy a wide depression region occurs in the case of the 5SiNT, while in the case of the 6SiNT this depression is more narrow. The presence of the depression zone is supported by the LDOS.

The LDOS for the highest occupied molecular orbital (HOMO) of the 5SiNT specie consists of charge concentration between atoms of the same transversal section of the tube, and small bridges between similar atoms from different pentagonal rings. The LUMO states are concentrated in smaller rings also between atoms from same pentagonal ring but without any connection between the rings.

In the case of the 6SiNT, the HOMO presents an uniform charge distribution along the Si-Si bonds, while in the case of the LUMO this distribution is localized only on half of the tubes lengths.

As a conclusion, bridges between the pentagonal and hexagonal rings exist in both cases, especially in the case of HOMOs, which supports the non-zero density at the Fermi energy. But these bridges are present only in the case of the LUMO of the 6SiNT, which explains the small energy needed to allow conduction, or in other words, the small energy gap.

Also a strong localization can be seen only in the case of the 5SiNT, as the most charge is distributed on the pentagonal rings, and not between them. In the case of the 6SiNT, the charges no strong localization is seen.

2.4 The vibrational density of states

The phonon band structure proves to be a very effective tool for the study of stability of periodic structures. If all the vibrational modes of a crystal are associated with a positive eigenvalue of the dynamical matrix, all the collective displacements of the atoms, or change of unit cells, increase its energy the crystal is stable against all possible infinitesimal collective changes of its structure. An energy barrier separates this phase from other possible energetically favored phases. The full phonon band structure provides an unique and complete characterization of the (meta)stability of a phase.

The phonon dispersion curves obtained for 5SiNT and 6SiNT are given in the right panels of Fig. 2.3, while the corresponding VbDOS are presented in the left panels. We note that no negative frequencies are present in the phononic band structure. This is a clear indication for the stability of both structures. The main features of VbDOS for 5- and 6SiNTs are in qualitative agreement with the VbDOS for Si nanowires reported by Peelaers *et al.* [14]. In particular, two local maxima of the VbDOS are found at 90 cm^{-1} (acoustic modes) and 344 cm^{-1} (optical modes) for 5SiNT, and at 83 cm^{-1} and 312 cm^{-1} for 6SiNT, respectively.

Next, we project the vibrational eigenvectors onto the z-axis (i.e. parallel to the nanotube). The VbDOS of the resulting z-projected eigenvectors is then constructed.

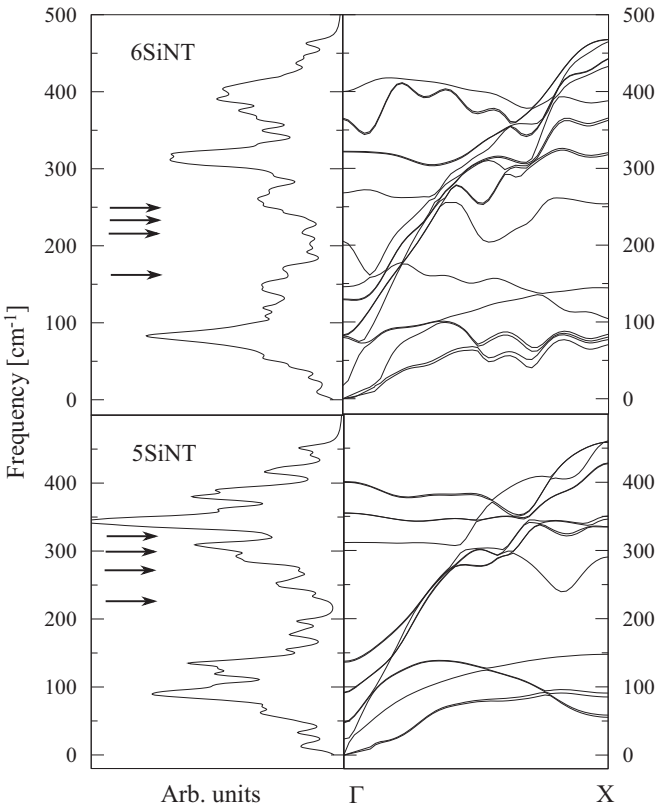

Figure 2.3: Phononic band structure and the vibrational density of states for the 5SiNT and 6SiNT. Breathing modes are indicated by arrows.

The results of our analysis are presented in Fig. 2.4. We note that transverse modes are dominant in the region 0-70 cm^{-1}, while the longitudinal ones are dominant at large frequencies (i.e. above 425 cm^{-1}). The two local maxima of the VbDOS mentioned above are dominated by transverse modes. In the case of 5SiNT we note the presence of a gap in the transverse VbDOS, between 190 and 210 cm^{-1}; no such gap is present for 6SiNT.

2.5 Isotopic substitution

Finally, we investigated the effect of isotopic substitution upon the VbDOS of the studied SiNTs. We consider that the layers of the SiNT's are formed either by ^{28}Si atoms (i.e. the most abundant isotope of the silicon [15]), either by ^{30}Si atoms (see also Fig. 2.1 for an intuitive representation). We choose the ^{30}Si isotope because it has the largest mass among the stable isotopes of the silicon and about 3% natural abundance [15]. In the case of ^{29}Si doping we get similar but less pronounced trends.

In the presence of isotopic substitutions, both systems exhibit a depletion of the VbDOS peaks in the region 300-400 cm^{-1}. The magnitude of these changes depends on the number of isotopically substituted layers. Precisely, for a substitution with less then 38% and 47% of the total number of atoms for the 5SinT and 6SiNT, respectively, no

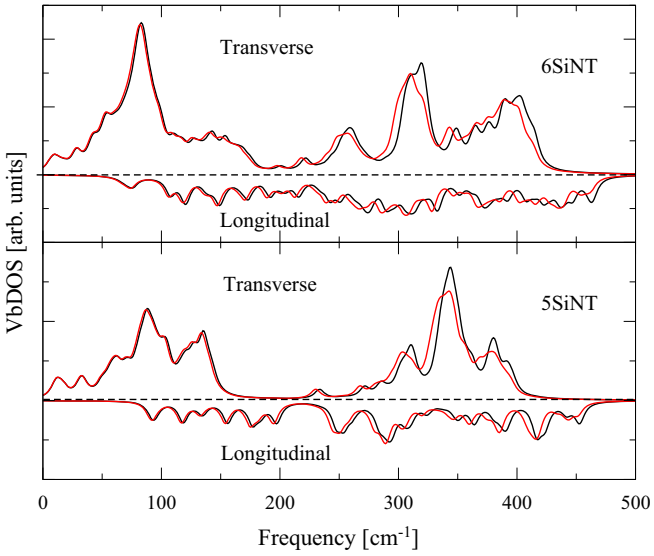

Figure 2.4: Comparison between the total, transverse and longitudinal VbDOS for 5SiNT (bottom) and 6SiNT (top). The effect of the isotopic substitution upon the total and longitudinal VbDOS is also presented: black curves - results for nanotubes including only ^{28}Si; red curves - results for nanotubes isotopically doped with ^{30}Si (see text for details).

important changes are visible; if however, the substitution ration is more than the above values, a reduction with 20% in the amplitude of the largest peaks occurs (see Fig. 2.4). These results are in good agreement with the predictions of the vibrational Hamiltonian of a diatomic lattice model.

2.6 Conclusions

We studied the phonon spectrum for two types of single walled silicon nanotubes, by performing ab initio calculations (DFT). Our results indicate that the two structures are stable (i.e. no imaginary frequencies are present in the phonon spectra). We show that the vibrational density of states for 5- and 6SiNT display similar features with those of the more complex silicon nanowires [14]. We also investigated the effect of the controlled isotopic substitutions upon the vibrational density of states. We found that, for both types of nanotubes, a relative important depletion of the VbDOS occurs for frequencies ranging from 300 to 400 cm^{-1}. We have shown that the simple model of vibrational Hamiltonian for diatomic 1D lattice can be used to explain this behavior. Therefore, our conclusion is that the changes of VbDOS are most important when the number of isotopically substituted layers is close to the number of ^{28}Si layers.

Chapter 3

Spin crossover molecules

3.1 Pre adsorption study - the isolated molecule and its distortion

The behaviour of spin crossover compounds is among the most striking and fascinating shown by relatively simple molecular species.[16] Coordination compounds of transition metal ions may, under certain conditions, exhibit a switching phenomenon, where the central metal ion changes the spin state upon a change of temperature, application of pressure, irradiation with light, or in a magnetic field. This phenomenon is known as spin transition (ST) or spin crossover (SCO). The change of spin state is accompanied by a change of electronic structure of the central ion and the complex molecule on the whole, which changes markedly the physical and chemical properties of the substance.

Octahedral complexes of d^{4-7} ions may be either high spin (HS) or low spin (LS), depending on whether the ligand field strength Δ (the electrostatic field acting at the central metal ion) is weaker or stronger, respectively, than the spin pairing energy [17]. In weak fields (see Fig. 3.1) the ground state is HS where the spin multiplicity is a maximum, the d electrons being distributed over the t_{2g} and e_g sets whereas strong fields stabilise the LS state with minimum multiplicity, the t_{2g} set being completely occupied before electrons are added to the e_g set[16]

Recent experiments [18, 19] have shown that strong coupling to a metallic substrate inhibits the switching ability between the two magnetic states, while weak coupling maintains the molecule bistable, although temperature cannot be any longer used to induce the spin transition. Here we consider one of the SCO prototype, Fe(1,10-phenanthroline)$_2$ (NCS)$_2$ [or cis-bis (thiocyanato) bis (1,10-phenanthroline)-iron(II)] from now on Fe-phen (see Fig. 3.2), and explore the relation between the molecule geometry and possible distortions arising from the interaction with a substrate. In order to mimic the interaction with a surface we studied the electronic and structural properties of such molecule by varying the distance between the two S atoms, d_{SS}, which are used to bind it to the

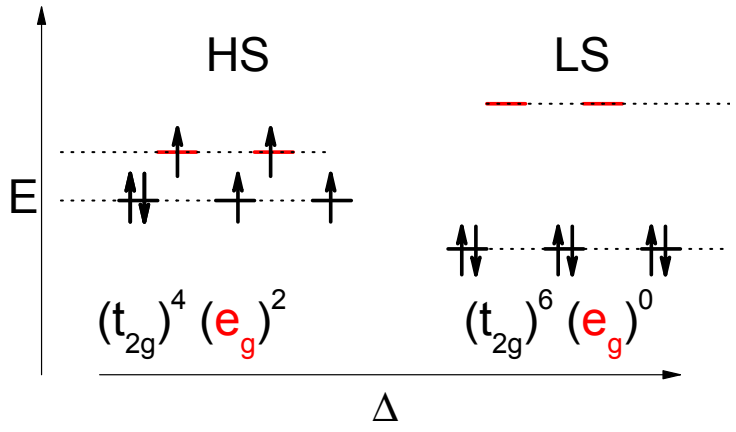

Figure 3.1: Electronic configuration for a d^6 iron(II) ion, in the HS state and in the LS state.

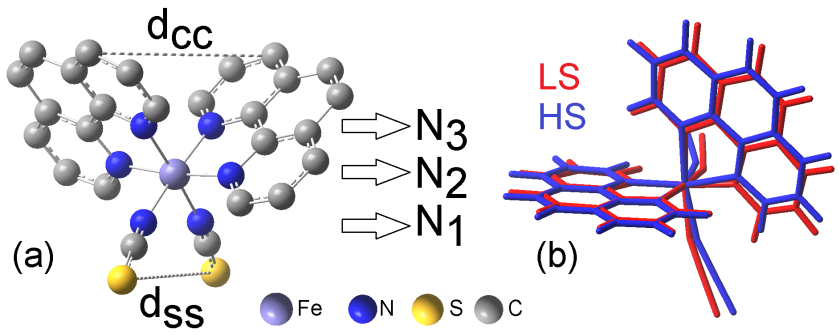

Figure 3.2: The optimized geometry of Fe-phen in LS state (a) and the structural difference between HS and LS (b). (For clarity, in panel (a) the H atoms are not draw). The S-S distance, d_{SS}, and the C-C distance, d_{CC} are also indicated. Note that in the HS state there is an elongation and a distortion of the first coordination shell. In the molecule we have three inequivalent pairs of N atoms, namely the ones residing on the SCN arms (N_1), those forming the horizontal Fe-N bond (N_2) and those heading upwards (N_3).

substrate. The sulphur based adsorption is suggested by experimental data.[18]

The geometry of the two spin states of Fe-phen were relaxed using both the SIESTA [10] and the GAUSSIAN09 code [13]. The SIESTA code implements norm-conserving Trouillier-Martins pseudopotentials. For the SIESTA calculations a double-ζ polarized basis set and the PBE exchange-correlation functional [12] were employed, with the molecule placed in a cubic box 70 Å in side. Calculations performed with GAUSSIAN09 used the TZVP [21] basis sets with the B3LYP [20] exchange-correlation functional. All the calculations were done without imposing any symmetry.

Distorted configurations, simulating the interaction with a substrate, were obtained by increasing the S-Fe-S angle, modifying also the angle between the entire thiocyanate arms (SCN arms). This produces a different d_{SS}. Then the molecules were allowed to relax except for the S atoms, which were kept fixed at their original positions. Relaxation

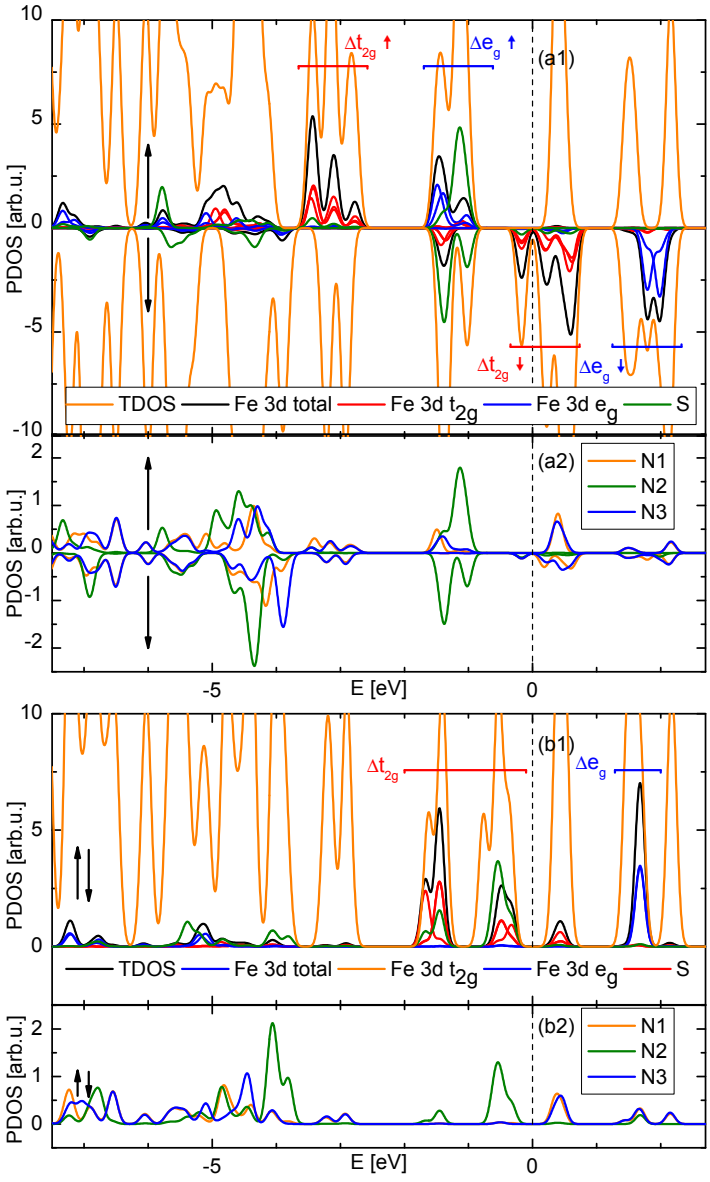

Figure 3.3: PDOS and TDOS for the HS (upper panel) and LS (lower panel) states of Fe-phen, computed using the PBE functional. For each panel the lower graph is a zoom over the N PDOS. The dotted line is the energy at the neutrality point, taken at 0 eV.

was done with conjugate gradient until the forces were smaller than 0.05 eV/Å.

The geometry of the undistorted gas phase molecule are in good agreement with the experimental [22] and other theoretical results from the literature [23, 24].

Our results show that the B3LYP hybrid functional tends to stabilize the HS configuration as the ground state, while local and semi-local functionals, as PBE, favour the LS one (this trend was also observed in other theoretical works like Ref [25], [23] and [26]). The latter result is in agreement with experimental evidence. This however, should not be taken as a proof of the goodness of local and semi-local functionals for this problem, since for a true estimate of the relative stability of the two magnetic phases intermolecular interaction should be taken into account [26].

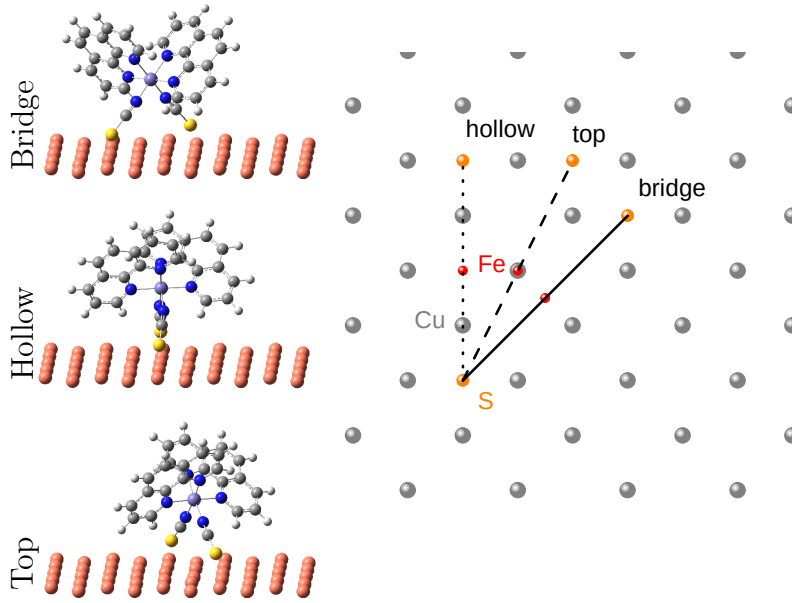

Figure 3.4: The schematic representation of the adsorption geometries studied for the Cu (100) substrate. Due to the symmetry of the metallic substrate and due to the preference of the S to adsorb on hollow position, the number of possible configurations is reduced to three representative configurations.

The electronic structure of the undistorted molecule, more precisely the projected (PDOS) and total density of states (TDOS), computed with the PBE functional included in the SIESTA code, are shown in Fig. 3.3[27]. In general the SCO transition is responsible for a redistribution of the occupancy of the Fe $3d$ shell (Fe^{2+} with d^6 configuration). In the LS case the t_{2g} levels are all doubly occupied, while the e_g remains empty (Fig. 3.3 (b2)), leading to a spin $S = 0$. In contrast in the HS configuration (Fig. 3.3 (b1)) two electrons are removed from the t_{2g} levels and placed, with opposite spin in the e_g. Thus one remains with a fully spin-polarized e_g shell and with four electrons in the t_{2g} for a total spin of $S = 2$. This is perfectly consistent with both the experimental evidence and many published theoretical works. [28, 29]

Our results concerning the geometrical reorganization of the molecule due to the d_{SS}-based distortion, show (1) negligible variations in the opening of the phenanthroline lobes (PLs) which do not support an scissors-like distortion (i.e. the increase/decrease of the thiocianato's (SCN) opening induces an increase/decrease of the PLs opening, and vice versa) for the gas-phase molecule and (2) the best description of the geometry is obtained based on PLs dynamics and not based on Fe's contributions to PLs opening.

The geometry and energy variations of the Fe-phen with respect to the d_{SS} parameter, together with the small number of atoms involved in sulphur-sulphur distortions, allow us to propose the sulphur based adsorption mechanism as a main adsorption mechanism for the Fe-phen molecule on metallic substrates. On the other hand, the PL based adsorption would imply bigger structural changes (deviations from the planar geometry of the multi-

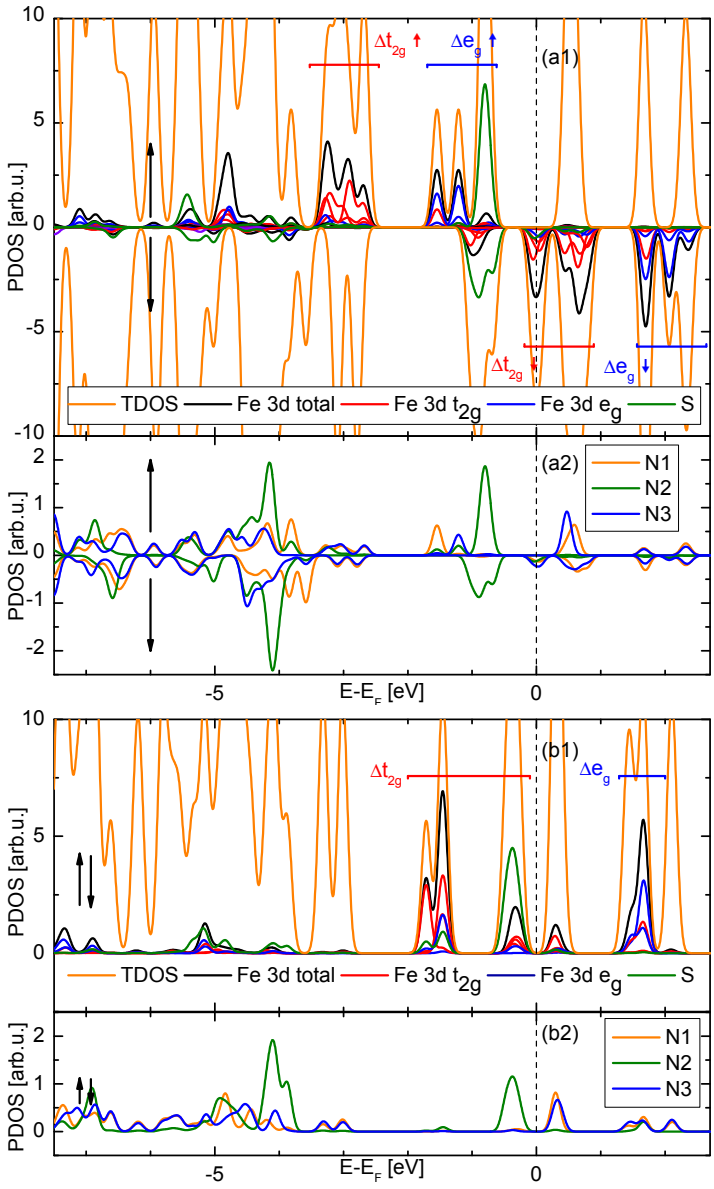

Figure 3.5: PDOS and TDOS for the HS (upper panel) and LS (lower panel) states of Fe-phen adsorbed on the Cu (100) surface in top position. For each panel the lower graph is a zoom over the N PDOS.

benzene rings) accompanied with higher energy variations.

3.2 Adsorption on Cu(100) surface

Based on the results from the previous chapter we have studied the adsorption of Fe-phen molecule on Cu(100) surface; only geometries with the S atom in hollow Cu positions have been considered. The PLs based adsorption, was found not to be energetically favoured at the PBE level of theory. The final geometries and their relation with the symmetry of the Cu (100) surface are shown in Fig. 3.4.

From the energetic point of view the top position is found to be the most stable one.

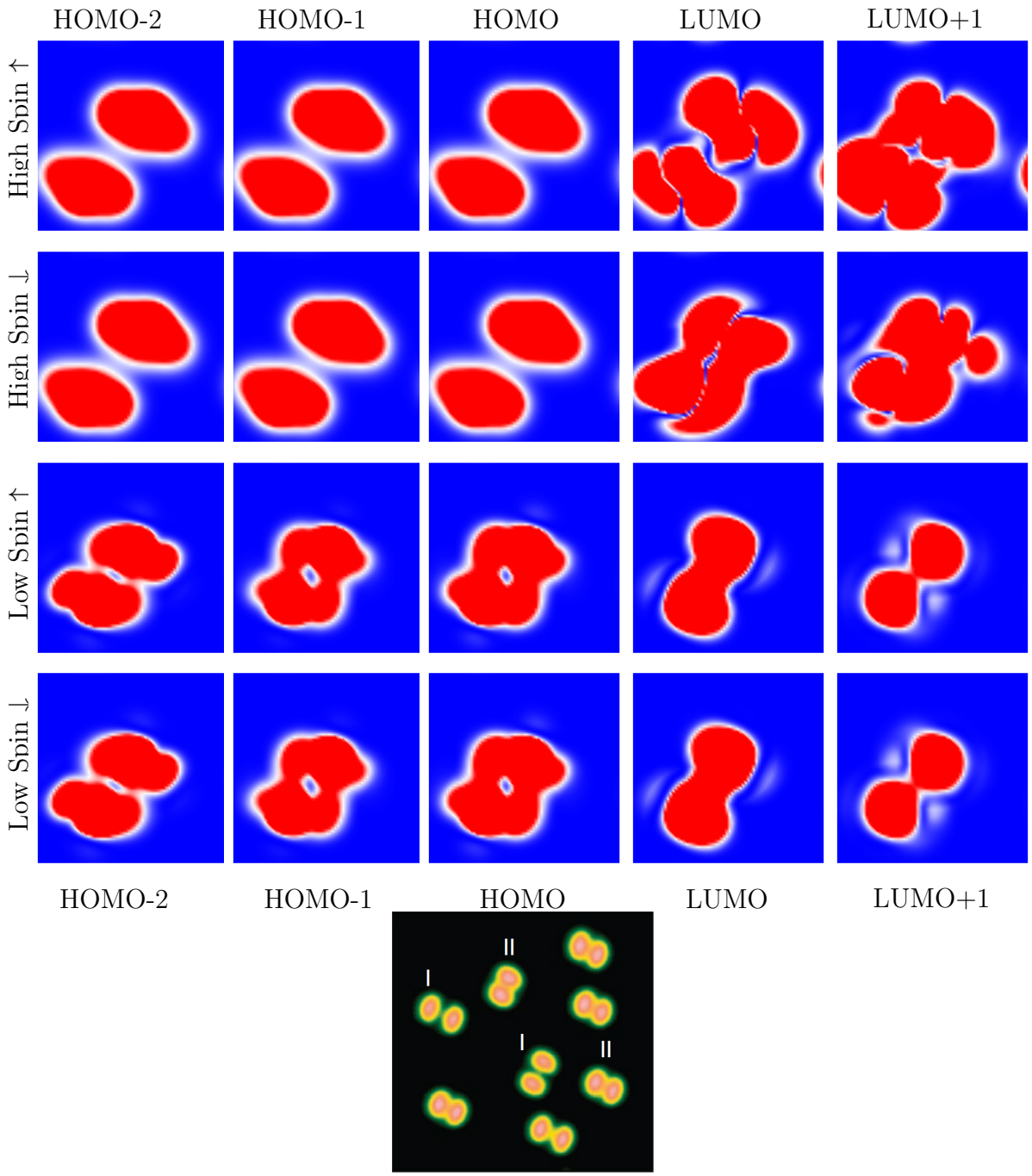

Figure 3.6: Simulated STM images for the adsorbed Fe-phen molecules on top configuration. The bottom image is an experimental STM image[18] of the isolated Fe-phen molecules on the Cu(100) surface with two conformations denoted as I (HS) and II (LS).

The density of states for the molecule adsorbed in this configuration is shown in Fig. 3.5. As expected in the case of adsorption, the most important changes in the PDOS are the widening of the peaks.

The computed STM images, are in good agreement with the experimental results [18], which show wider openings of the PLs in the case of HS state compared to the LS state.

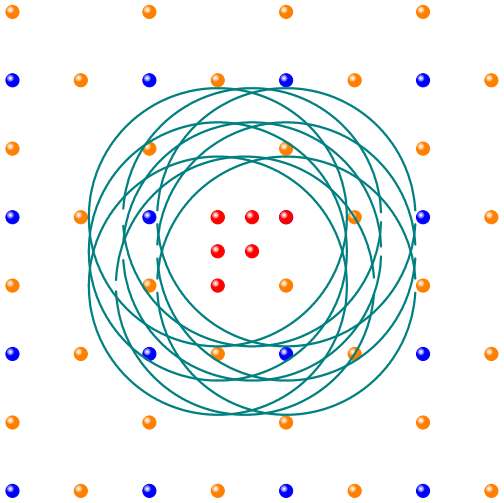

Figure 3.7: The schematic representation of the adsorption geometries studied for the CuN (100) substrate (left). Only systems consisting of S atoms adsorbed on hollow position, or with various N and Cu neighbours were considered (i.e. systems for which the S atoms are on the green circles and are at the same distance from the substrate). In total, a number of 26 possible configurations have been studied. The position of the Fe atoms is represented by the red dots.

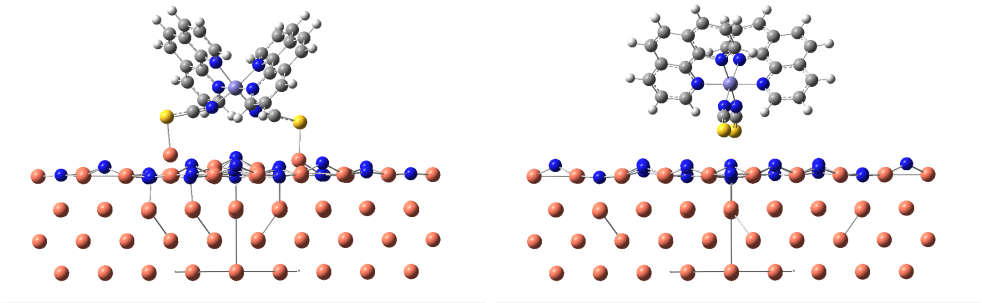

Figure 3.8: The geometries for the configurations 1 (left) and 26 (right).

3.3 Adsorption on CuN/Cu(100) surface

Considering a S-based adsorption and based on the symmetry of the CuN/Cu(100) surface (see Fig. 3.7), a number of 26 possible configurations are studied LS state. The most stable configurations are shown in Fig. 3.8.

The PDOS of both LS state (Config.no.26 and Config.no.1) are presented in Fig. 3.9. Comparing the PDOS for these two species, one can remark that the gap between the main two areas from the Δt_{2g} is smaller in the case of Config.no.1. Also, the gap between the higher energy are from Δt_{2g} and the next unoccupied domain is constant in for the two species. In the case of the Config.no.1 the height of the peaks of the Fe orbitals are slightly smaller compared to those of Config.no.26, the only exception being the higher

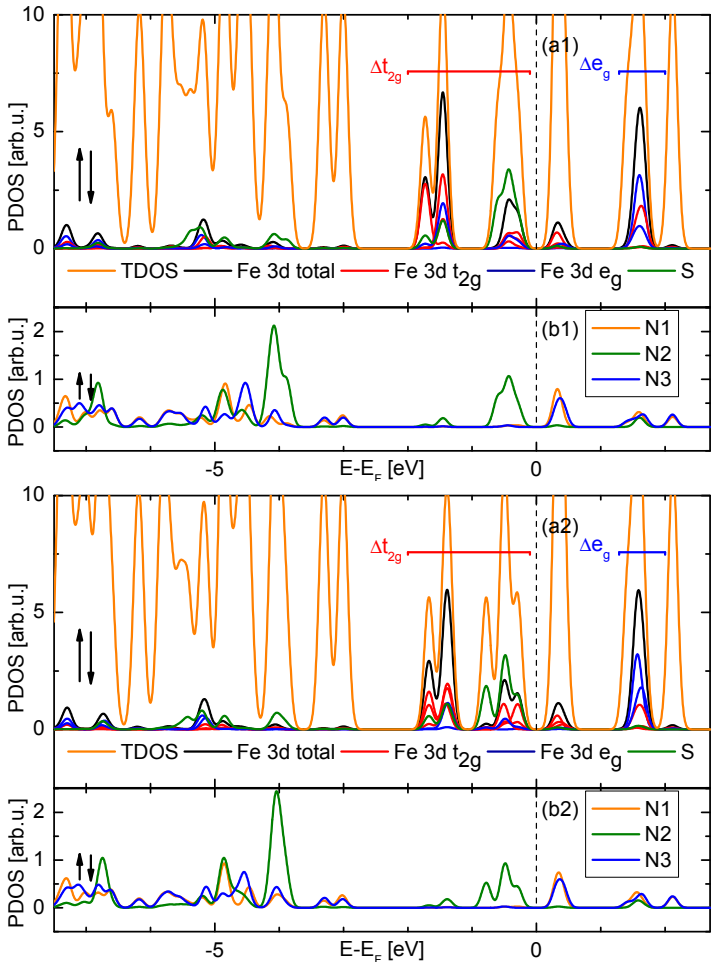

Figure 3.9: PDOS and TDOS for the LS Config.no.26 (upper panel) and Config.no.1 (lower panel) states of Fe-phen adsorbed on the CuN/Cu(100) surface in top position. For each panel the lower graph is a zoom over the N PDOS.

energy sub-domain from the Δt_{2g} domain. In the case of Config.no.26 we also have a more pronounced contamination from the e_g in the Δt_{2g} domain, compared to the Config.no.1. In the Δe_g domain, in the case of Config.no.1 there is smaller contamination from the t_{2g} orbitals, compared with the case of Config.no.26. These contaminations are due to the coupling with the substrate.

Excluding the $3d$ mixing due to the coupling to the substrate, the Fe PDOS is closest to the molecular PDOS, in the case of the Config.no.26. The only noticeable difference is the small widening of the found in the case of the adsorbed system.

The experimental STM images show two lobes either connected through with a central feature (in the case of the HS) ar with very reduced or no features (in the case of LS). Our simulated STM images (see Fig. 3.10), are similar with the afore mentioned features, the highest similarity coming from the HOMO and LUMOs orbitals. Some images from the experimental data (from [18]) also show small misalignments perpedicular to the axis which connects the two lobes. This are more proeminent in the case of HS. Same types

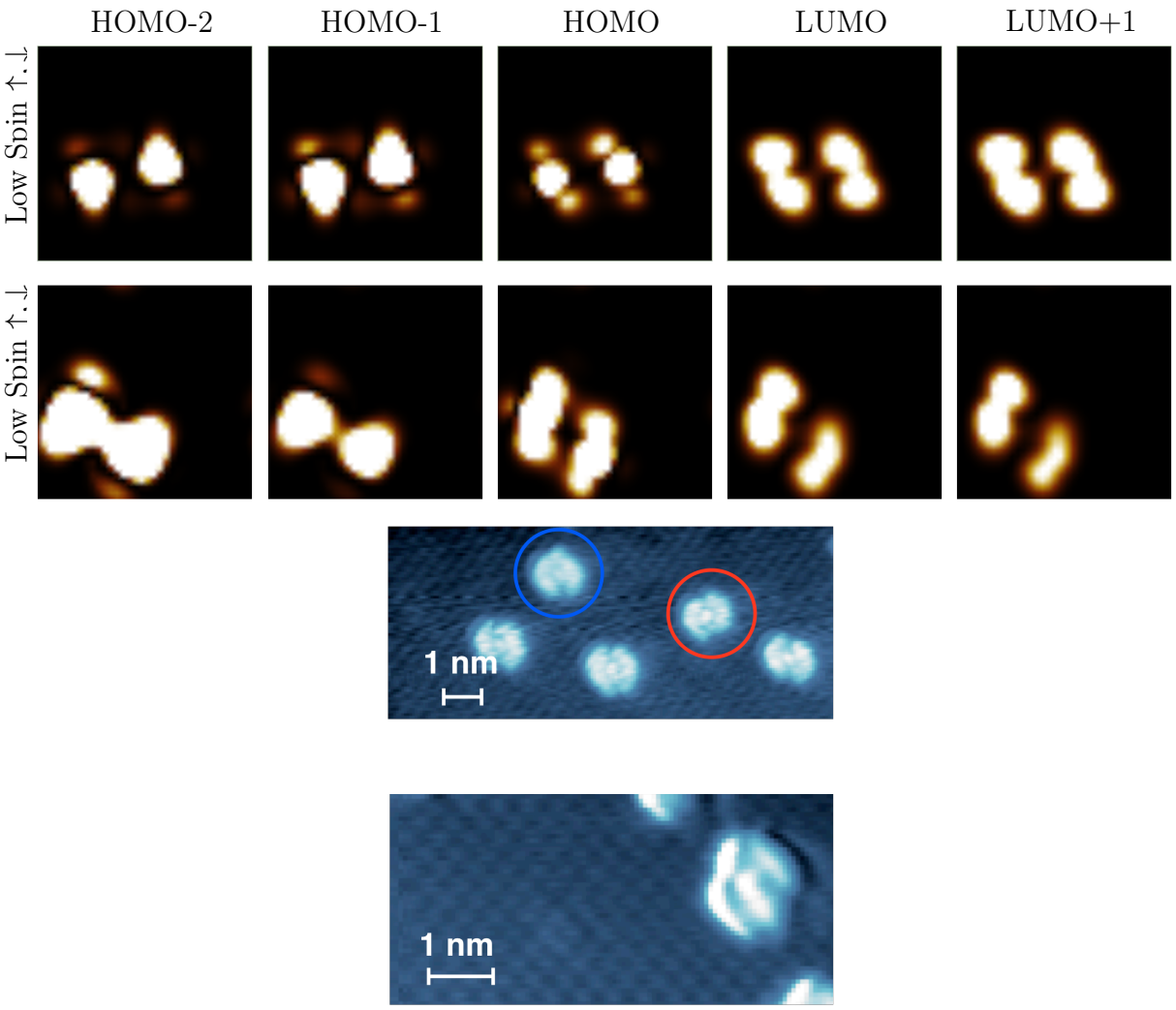

Figure 3.10: The STM images computed for the Config.no.26 (top row) and for the Config.no.1 (middle row). The bottom two images show the experimental STM image of Fe-phen single molecules adsorbed on the CuN/Cu(100) surface. The molecule encircled by red (blue) is in the HS (LS) state.

of misalignment are present also in our computed STM images.

3.4 Conclusions

From electronic structure point of view, the N_2 atoms have a strong influence on both the stability of and the transition between spin states, as they generate a symmetric field to the Fe ion. The fields generated by the N_1 and N_3 atoms lack this symmetry, thus their contributions to the PDOS lies at either very low energies, either to unoccupied molecular states.

The structure of Fe-phen is shown to have a great flexibility, in the sense that the change in the opening angle of the SCN arms, (1) increases slightly the energy of the distorted system, for a large range of d_{SS}, (2)doesn't influence the dynamics of the PLs.

The adsorption on the Cu (100) surface was studied using the framework of standard DFT, and provides the following insights: (1) the adsorption of the Fe-phen molecules is more energetically favoured through S atoms, rather than PLs, (2) the adsorption of the Fe-phen molecule is not spin dependent, in the sense that there no configurations favourable to only a certain spin state, (3) the adsorption mainly occurs with the Fe atom on top of a Cu from the substrate, (4) the energy difference between the possible configurations it is shown does not allow the transition from one configuration to another even at room temperature.

Insights into the structure of CuN/Cu(100) substrate were made, showing that the N atoms have a slighty higher height than the Cu atoms. No buckling or oscilating N heights are observed.

The adsorption on the CuN/Cu(100) surface was studied through scanning both vertically and in configurational space. The main conclusion is that the S-based adsorption mechanism relies on close proximity of S atoms to Cu atoms. As in the case of adsorption on the Cu(100) surface, the adsorption is not spin-dependent. We have studied the most energetically favoured configurations (from the results provided by the energy scans) and found that Config.no.1 is one of the most stable of them. The adsorption properties show that the coordination sphere of the Fe atom is very similar to that of the isolated (gas-phase) molecule. The adsorption properties (i.e. the STM images) confirm that the studied geometries are very close to experimental ones.

Chapter 4

DFT and DFT-D study of Lutetium bisphthalocianines complex

4.1 Introduction

The class of phthalocyanines (Pc) still presents nowadays very high scientific interest due to their unusual physical and chemical properties and to their promising applications in science and technology [30]. The most important properties that these compounds possess are the structural similarities with chlorophyll and with porphyrins, which make them very adequate for applications in nanoelectronics, the artificial conversion of solar energy into electric energy[31] and for spintronics applications.

A special place between metallic substituted Pcs is held by the Lutetium (III) bisphthalocyanine ($LuPc_2$) shown in Fig. 4.1. It's synthesis was first reported in the mid 1960s by Moskalev *et al.*[32], but only after more than 20 years it was proved to be one of the first intrinsic molecular semiconductors discovered[33]. The molecular complex is also a suitable candidate for applications in the field of nanoelectronics [30, 34].

The theoretical calculations were carried out using the GAUSSIAN 09 program package [13]. The functional used in order to determine the molecular and electronic structure of $LuPc_2$, as well as the normal modes of vibration, was the hybrid B3LYP in combination with the 6-31G(d) basis set for the C, H, O and N atoms. The CEP-121G and the SDD effective core potentials (ECPs) were used to describe the effect of the core electrons for the Lutetium atoms. Two types of calculations were performed; the first relies on standard Density Functional Theory (DFT) methods, while the second methodology is based on DFT with dispersion corrections using Carbon atom centered effective core potential (DFT-DCPs) [35]. DFT-DCP calculations were performed using the B97-1[36] functional, which it is based on the well known B97-D[37] functional

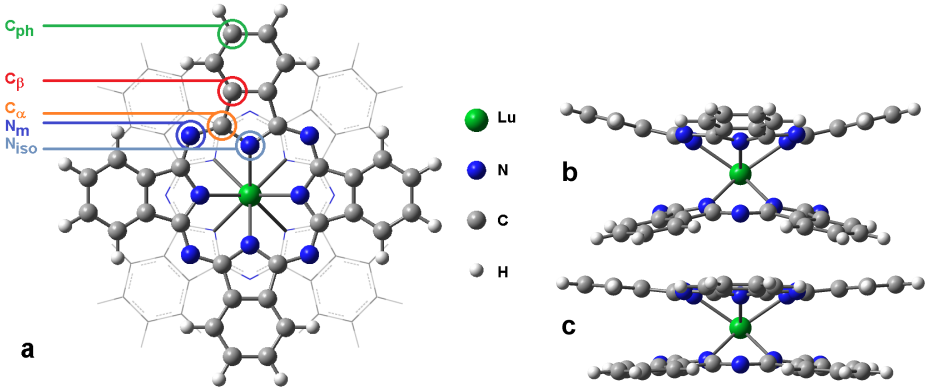

Figure 4.1: Optimized geometry of $[Lu(Pc)_2]$ (D_{4d} symmetry; view along the C_4 axis (a) and side view of the B3LYP and B97-1 structures (b and c, respectively)).

	$LuPc_2$ B971 SDD	$LuPc_2$ B3LYP SDD	$LuPc_2$ B971 CEP	$LuPc_2$ B3LYP CEP	$[LuPc_2]^-$ B971 SDD	$[LuPc_2]^-$ B3LYP SDD	$[LuPc_2]^-$ B971 CEP	$[LuPc_2]^-$ B3LYP CEP
Lu - N_{iso}	2.396	2.413	2.414	2.432	2.410	2.431	2.427	2.451
Pc -Pc	2.706	2.730	2.746	2.778	2.736	2.771	2.775	2.826
N_{iso}-Lu-N_{iso}	111.3	71.3	110.7	71.0	110.9	71.0	110.3	71.6
γ	6.0	14.2	5.75	14.3	7.1	15.2	6.9	15.2
δ	174.0	165.8	174.25	165.7	172.9	164.8	173.1	164.8

Table 4.1: Optimized and experimental bond lengths and valence angles of the neutral and anionic forms of $LuPc_2$, obtained at the B3LYP/6-31G(d) and B97D-DCP/6-31G(d) levels of theory, with SDD and CEP-121G ECPs for the Lu atom.

4.2 Optimized geometry

Regarding the optimize geometry of the $LuPc_2$, it should be noted that the bond lengths calculated using the two ECPs are comparable, significant differences arising only in the case of the interplanar distances (the distance between the inversion centers of the phthalocyanine rings, Pc-Pc). Furthermore, important differences between anion and neutral complex are mostly observed in what concerns the same interplanar distance, the value for the anion being on average 0.0445 Å larger than the same distance for the neutral complex. As compared to the experimental values, the calculated bond lengths for both the $[LuPc_2]^-$ and $LuPc_2$ are with 0.01-0.02 Å larger. The interplanar distances are reproduced with greater accuracy by the SDD pseudopotential, but the overestimation is still important.

Concerning the differences between the non and dispersion corrected DFT methods, it should be noted that the DFT-DCP method generally gives rise to larger bond lengths. The two exceptions are the Lu-N_{iso} bond and the interplanar length which are closer to experimental values, the overestimation being more important in case of the anionic form.

The optimized structure contains two Pc planes that are bent outwards to the same

degree. This theoretical result is in agreement with X-ray diffraction experiments [38] and sustains the idea that the unpaired electron of the neutral complex is delocalized over the entire molecular complex.

Another important aspect is related to the doming of the $LuPc_2$ molecule, expressed in terms of the N_{iso}-Lu-N_{iso} angle. The C-pots method gives rise to two Pc rings less bent outwards than the normal SDD and CEP-121G calculations. For the comparison with other theoretical results, the angle δ was computed as the angle between the N_{iso} atoms plane and each of the planar C_8N pyrrolic units. The results based on B97-1 functional are within 2° range compared to those from Ref. [39]. The B3LYP gives systematically smaller values which indicate a greater doming.

The bending of the isoindole rings, quantified by γ, gives in the case of B3LYP functional very close values to those reported by Bidermane *et al*[40]. The B97-1 results both for the neutral and anionic specie very close to the experimental ones which suggest modest bendings of the isoindole rings[38]. Also, Bidermane *et al.* suggested a intermolecular (van der Waals) contribution to the flatness (un-doming) of the Pcs. Flat Pcs are only obtained only if dispersion correction through CPots are added to the B97-1 results.

Taking into consideration the interplanar length, we may conclude that, from the point of view of the doming, the molecular geometry predicted by the C-pot method is closer to reality.

4.3 Vibrational analysis of $LuPc_2$

In this study[41] we tested the utility of dispersion corrected potentials for predicting the vibrational data for $LnPc_2$ double decked, particularly for LuPc2 complex. Such a study is useful not only for a clear and reliable assignment of the normal modes of the single molecule but also for identifying the IR or Raman bands that can be used for the explanation of the orientation of the molecules on substrates or for the self-assembly of molecules when thin films are formed.

In order to correlate the experimental vibrational data for $LuPc_2$ with the theoretical results we used the IR data reported by Lu *et al.* [30] and Raman data obtained on $LuPc_2$ thin films given by Zahn and collaborators [42].

Before proceeding to the assignment of vibrational spectra of $LuPc_2$ we tested the B971-DCP methodology on $TmPc_2$ compound for which reliable IR and Raman data have been reported by Moreira and Aroca [43]. The geometry of the complex with a C_{2v} symmetry was optimized using the B971-DCP/6-31G(d) with SDD ECPs for Tm atom. We found that the B971-DCP/6-31G(d)-SDD methodology is feasible for the calculation of IR and Raman spectra of for $TmPc_2$ Thus, we used the same approach for the calculation of $LuPc_2$ compound. In case of $LuPc_2$ compound we used also the B3LYP/6-31G(d)-SDD level of theory for the calculation of vibrational spectra. It is important to note that the

optimized geometry at this level of theory shows a much more pronounced doming than in the case of B971-DCP/6-31G(d)-SDD method (see Fig. 4.1).

Table 4.2 and 4.3 summarizes the most important vibrational IR and Raman bands of the $LuPc_2$ complex, together with the calculated wavenumbers and normal modes assignments suggested by DFT results. As easily can be seen in this table, the predicted B971-DCP/6-31G(d)-SDD theoretical values are in consistently good agreement with the experimental values. The average of the deviations between the RR 676.4 nm experimental data and theoretical values is 3.3 cm^{-1}, while the standard deviation of residuals is 9.0 cm^{-1} when the 9-parameters ESFF procedure is used.

Raman spectrum of $LuPc_2$ powder has the most intense bands at 679, 741, 478, 576, 782 and 815 cm^{-1}. This is similar to the $TmPc_2$ case where the resonant spectrum shown bands with appreciable intensity in the low wavenumber region. While the relative intensities and their positions are well reproduced for these bands at 696, 756, 487, 592, 772, and 835 cm^{-1}, however we have to note that the most intense Raman bands are predicted at 1537, 1324, 1305, 1077 and 1017 cm^{-1} (see the assignments in Table 4.2 and 4.3). These predictions remains to be confronted with new experimental Raman data obtained in non-resonant conditions.

The lutetium atom seems to be involved mainly in two vibrations: the first one has the calculated wavenumber at 242 cm^{-1}, in perfect agreement with the experimental value (242 cm^{-1}) and it is assigned to Lu-N_{iso} stretching vibration. The second one, observed experimentally at 286 cm^{-1} is a symmetrical bending of the Lu-N_{iso} bonds, with the calculated wavenumber at 294 cm^{-1} and the experimental counterpart at 286 cm^{-1}.

Concluding, we demonstrated that the B971-DCP/6-31G(d)-SDD approach is a reliable method not only for giving correct geometries for lanthanide-bisphthalocyanine compounds but also for spectroscopic data like infrared and Raman spectra. The IR spectra have been correctly reproduced, both in band positions and intensities. On the other hand, Raman intensities, being strongly affected by the laser excitation line have been reproduced only in a qualitative manner. Pre-resonant studies must be performed for a reliable prediction of band intensities in resonant conditions, such works being in progress at the moment.

4.4 Projected density of states

The unrestricted B3LYP PDOS of the $LuPc_2$ complex shows a region consisting of two shifted electronic levels around the HOMO-LUMO gap, for each spin polarization; the energetical spacing between these levels is different for each spin polarization. The levels present contributions only from C atoms. This mechanism of shifted and asymmetrical spaced levels allows the partial occupation of one orbital, in fact also suggested by the first experimental[44] results and the recent theoretical results[45].

Table 4.2: Selected experimental and B971/6-31G(d)-DCP-SDD calculated wave numbers of $LuPc_2$ complex.

Mode number	Symm.	Theoretical Data: Calculated wn [cm^{-1}]	I_{IR} [%]	I_R [%]	Scalling factor	Scalled wn [cm^{-1}]	Experimental Data: Ref. 1	Ref. 2	Assignments
1	A_1	211	0.00	1.41	0.9707	205		208	Pc stretching
2	A_1	249	0.05	11.58	0.9707	242		242	ν(Lu-N_{iso})
3	A_1	290	0.00	6.03	1.0122	294		286	$\delta_{sym}(LuN_8)$
4	A_1	359	0.01	0.79	0.9838	353		353	out of plane macrocyle def.
5	A_1	442	0.29	0.06	0.9838	435	427		out of phase isoindole def.
6	A_1	481	0.00	2.61	1.0122	487		478	in plane pyrrole def.
7	B_2	506	2.54	0.04	1.0122	512	501		δ(pyrrole-phenyl)
8	B_2	509	0.48	0.25	1.0122	515			δ(pyrrole-phenyl)
9	B_1	570	0.88	0.00	1.0122	577	562		in plane isoindole def.
10	A_1	583	0.12	1.46	1.0122	590	592	576	in phase Pc breathing
11	B_2	634	0.27	4.45	1.0122	642	628		in plane isoindole def.
12	A_1	688	0.50	7.32	1.0122	696	680	679	δ(CNC) + in plane phenyl def.
13	A_1	744	83.28	0.02	0.9838	732	727		in phase out of plane isoindole def. +ω (CH)
14	B_2	745	10.19	2.91	1.0122	754	741		in plane isoindole def.
15	A_2	747	0.01	14.53	1.0122	756		741	in plane isoindole def.
16	B_1	782	0.00	0.33	0.9838	769		770	out of plane Pc def.
17	A_1	785	3.39	6.25	0.9838	772		782	out of plane Pc def.
18	A_1	787	8.29	2.68	0.9838	774	780		out of plane Pc def.
19	A_1	818	7.78	0.23	1.0122	828	811		isoindole stretching
20	A_1	825	0.20	6.76	1.0122	835		815	in plane in phase 2Pc def.
21	B_1	883	0.63	0.03	0.9838	869	887		phenyl out of plane bending
22	A_1	946	0.37	0.17	0.9838	931	943	941	out of plane CH bending
23	B_1	1018	2.55	0.13	1.0122	1030	1009		δ(CCC) phenyl
24	B_1	1067	0.03	49.81	0.9532	1017		1006	ν(CN) pyrrole + δ(CCC) isoindole
25	B_2	1077	0.11	18.67	0.9532	1027		1030	ν(CN) pyrrole + δ(CCC) isoindole
26	A_1	1126	21.57	0.83	0.9532	1073	1062		pyrrole str. + ip phenyl def. + δ(CH)
27	B_2	1130	0.56	31.72	0.9532	1077		1104	pyrrole str. + ip phenyl def. + δ(CH)
28	B_1	1129	19.07	0.04	0.9724	1098	1116		δ(CH)
29	A_1	1159	0.00	15.55	0.9724	1127			δ(CH) + phenyl breathing
30	A_1	1177	0.01	6.03	0.9724	1144		1143	δ(CH) phenyl

Ref. 1 IR KBr pellets [30]; Ref. 2 RR 676.4 nm powder [42]; ν - stretch, δ - bending, ω - wagging, def. - deformation.

Table 4.3: Selected experimental and B971/6-31G(d)-DCP-SDD calculated wave numbers of $LuPc_2$ complex.

Mode number	Symm.	Theoretical Data: Calculated wn [cm^{-1}]	I_{IR} [%]	I_R [%]	Scalling factor	Scalled wn [cm^{-1}]	Experimental Data: Ref.1	Ref.2	Assignments
31	A_1	1189	0.00	10.03	0.9724	1156			δ(CH) phenyl + isoindole def.
32	B_1	1192	1.99	0.01	0.9724	1159	1161		δ(CH) + isoindole def.
33	A_1	1225	0.00	4.06	0.9724	1192		1214	δ(CH) + isoindole def.
34	B_1	1306	3.99	0.00	0.9724	1270	1283		δ(CH)
35	B_2	1334	100.00	0.30	0.9724	1297	1323		δ(CH) + δ(CNC) pyrrole + ν(CC) phenyl
36	A_1	1344	0.36	23.02	0.9707	1305		1301	phenyl stretch + pyrrole stretch + δ(CH)
37	A_1	1364	0.00	23.67	0.9707	1324		1330	phenyl stretch + pyrrole stretch + δ(CH)
38	A_1	1422	0.00	19.91	0.9532	1355		1345	ν(CC) + δ(CH)
39	B_2	1425	0.03	2.51	0.9532	1358			ν(CC) pyrrole + $\nu(CN_{aza})$ + δ(CH)
40	B_1	1429	9.00	0.02	0.9532	1362	1371		ν(CC) pyrrole + δ(CH)
41	A_1	1452	0.00	2.05	0.9707	1409			$\nu(CN_{aza})$ + δ(NCC) pyrrole
42	A_1	1471	0.00	5.48	0.9707	1428		1423	ν(CC) phenyl + δ(CH)
43	B_2	1479	0.20	2.04	0.9724	1438			δ(CH) + ν(CC) phenyl
44	B_2	1482	40.02	0.00	0.9707	1439	1454		$\nu(CN_{aza})$ + ν(CC) phenyl + δ(CH)
45	B_2	1525	0.08	12.97	0.9707	1480		1447	$\nu(CN_{aza})$ + δ(CNC) pyrrole + ν(CC) phenyl
46	A_1	1533	8.47	1.80	0.9707	1488	1490		$\nu(CN_{aza})$ + δ(CNC) pyrrole
47	A_1	1583	0.00	100.00	0.9707	1537	1521	1525	$\nu(CN_{aza})$
48	A_1	1611	2.42	0.05	0.9707	1564			ν(CC) + δ(CH)
49	B_1	1622	2.96	0.00	0.9707	1574			ν(CC) + δ(CH)
50	B_2	1622	3.07	0.00	0.9707	1574	1647		
51	B_2	3195	20.77	0.12	0.9578	3060	3052		ν(CH)
52	B_1	3215	13.00	0.06	0.9578	3080	3076		ν(CH)

Ref 1. IR KBr pellets [30]; Ref 2. RR 676.4 nm powder [42]; ν - stretch, δ - bending, ω - wagging, def. - deformation.

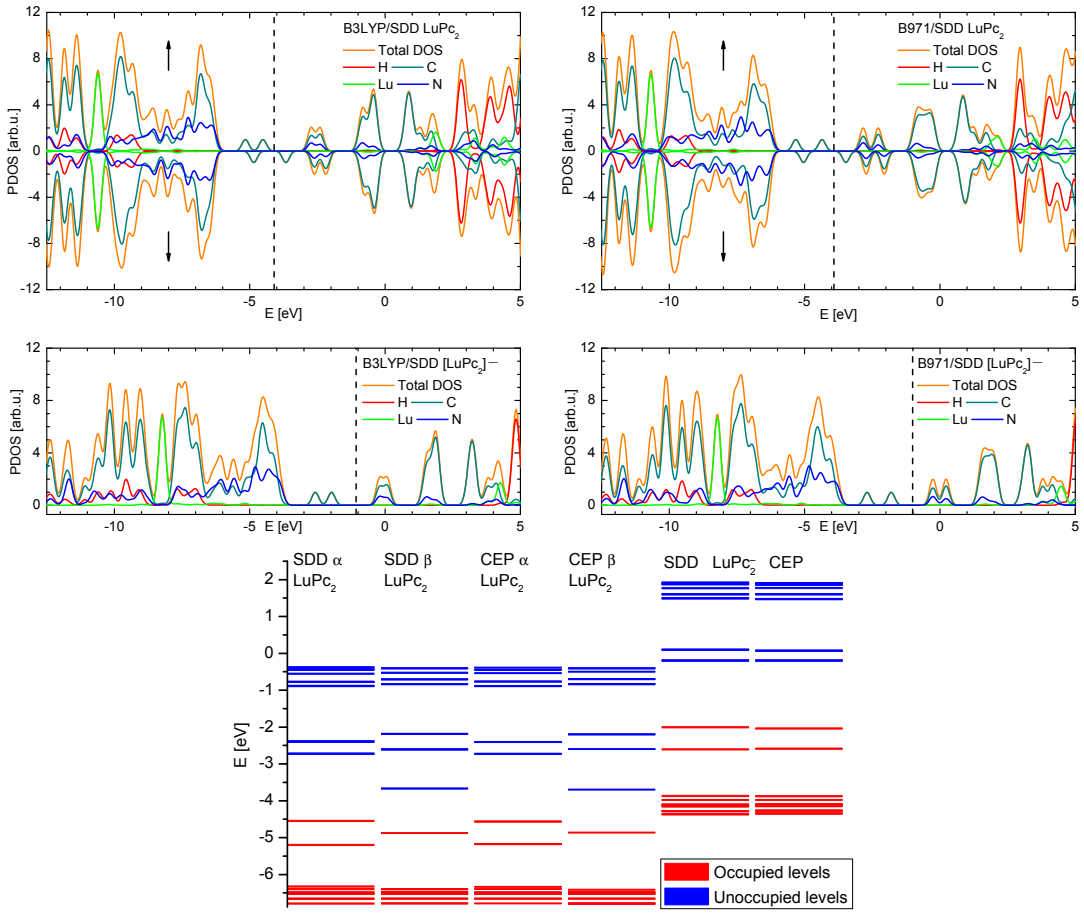

Figure 4.2: Projected density of states computed for the $LuPc_2$ complex (first row) and the anion (second row) using the B3LYP (left) and B971 (column) functionals for the SDD pseudopotential. The neutrality point is represented by the dashed line. For comparison, the orbital energies of $LuPc_2$ neutral and anion calculated with SDD and CEP ECPs for the Lu atom are shown in the bottom.

Also, the PDOS suggest very weak interactions between the Lu orbitals and those of C, N, below the neutrality point (i.e. the intermediate energy between the occupied states and the unoccupied states). A strong localization of Lu orbitals is present around ∼-10.5eV, when the SDD pseudopotential is used, while in the case of CEP pseudopotential this is shifted to ∼-16.5 eV. This shift can be explained by the fact that the CEP pseudopotential the $4s$, $4p$ and $4d$ Lu orbitals are included in the core[46], while in the case of the SDD pseudopotential these orbitals are treated explicitly and they are included in the valence shells[47]. Nevertheless, in both cases, these orbitals are almost chemically inert with very small superpositions with C and N orbitals. Above the neutrality point, some interactions between the Lu and C and N orbitals are present, but these less pronounced in the case of the CEP pseudopotential compared with the SDD pseudopotential. The weak interaction of the Lu atom with the N and C atoms and the contribution to low energy unoccupied MOs was also shown in Ref. [40].

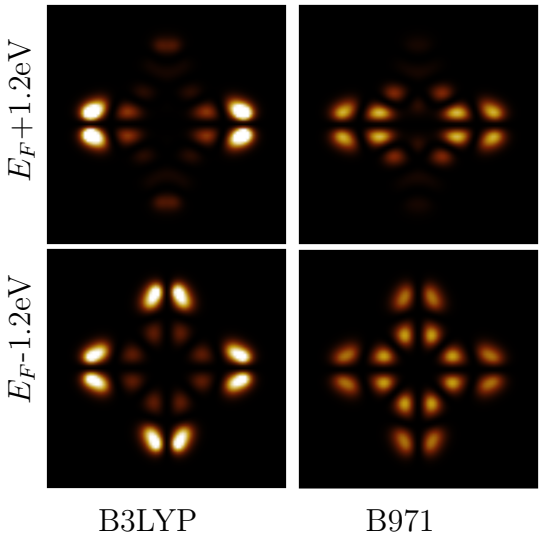

Figure 4.3: STM image for both filled and empty state for a bias voltage of 1.2 V.

4.5 STM images

STM images for the case of weak coupling to a metallic substrate have been obtained using the Tersoff-Hamann[48] approach for both B3LYP and B97-1 calculated structures. (The images obtained using either CEP-121G or SDD ECPs are identical.) The first noticeable difference between the STM images comes from the fact that B97-1 provides more uniform colour patterns. This is caused by the fact that this functional gives less distorted Pc rings, which in turn gives an almost constant interaction with the STM tip, whereas in the case of the B3LYP structure, the extremities of the Pc rings are closer to the STM tip, giving a more intense signal.

4.6 Conclusions

First of all, in what concerns the optimized molecular structures, we may conclude that the Lu atom has no relevant influence over the bond length and valence angles when comparing the $LuPc_2$ with the simple Pc molecule. Another important aspect to be mentioned is the fact that both Pc macrocycles bend to the same degree, confirming the hypothesis that the unpaired electron of the neutral system is delocalized over the whole molecule [49] and sustaining the experimental X-ray diffraction experiments [38].

There are no significant differences between the geometries of the neutral and anion molecular complexes. Both in the case of bond lengths, bond angles and dihedrals, $LuPc_2$ and $[LuPc_2]^-$ are comparable, the most significant difference arising only regarding the interplanar Pc-Pc distance.

Last, but not least, we also observed a decrease in the doming when using the B97-1 functional, as for regular DFT calculations. Moreover the Pc-Pc distance is closer to

experimental values, leading us to the conclusion that the C-pots method gives better results for this type of molecular complexes.

In the matter of the IR and Raman spectra, the $LuPc_2$ bands generally reproduce the ones computed for the Phthalocyanine (Pc) molecule, substantial differences being observed only in what concerns the band intensities. As such, we may first of all conclude that there are no important vibrations that involve the Lutetium atom, and second of all, we may say that the increase in intensity is due to the fact that the molecular complex contains two phthalocyanine rings. The vibrations giving rise to bands in the IR and Raman spectra are vibrations in the phthalocyanine rings. We also observe more intense bands in the IR spectrum of the $LuPc_2$ anion

We should also note that the present study is not exhaustive and there are some aspects that should be included in a future study. It is well known the fact that the $LuPc_2$ molecular complex presents itself under multiple oxidative states (..., $[LuPc_2]^-$, $LuPc_2$, $[LuPc_2]^+$, ...) and therefore it could be used successfully in electronic device that would function according to non-binary logics [50]. As a consequence, it would be useful to study from a theoretical and experimental point of view, not only the $LuPc_2$ neutral and anion, but also the $LuPc_2$ cation.

Final conclusions

By using the Density Functional Theory (DFT) we analyzed the vibrational properties of silicon single walled nanotubes. The motivation of the present work comes form a recent study of Bai et al., showing that such nanostructures can display a metallic behaviour. While experimental studies in the field are in an incipient phase, such findings suggests already several possible applications. Among them, the realization of systems with high electric conductivity, yet with relative reduced thermal conductivity is particularly attractive. Precisely, such structures may be ideal candidates for building eficient thermoelectric elements able to convert directly the thermal energy into electricity. In order to achieve such goal, the full understanding of the vibrational properties of silicon nanotubes is of capital importance, since the thermal transport is directly related to the vibrational properties and the electron-phonon coupling. As final results, we present the phonon band structure, vibrational density of states for three types of silicon single walled nanotubes.

Concerning the Fe-phen molecule, from electronic structure point of view, the N_2 atoms have a strong influence on both the stability of and the transition between spin states, as they generate a symmetric field to the Fe ion. The fields generated by the N_1 and N_3 atoms lack this symmetry, thus their contributions to the PDOS lies at either very low energies, either to unoccupied molecular states.

The structure of Fe-phen is shown to have a great flexibility, in the sense that the change in the opening angle of the SCN arms, (1) changes in a negligible measure the energy of the distorted system, for a large range of d_{SS}, (2)doesn't influence the dynamics of the PLs.

The adsorption on the Cu (100) surface was studied using the framework of standard DFT, and provides the following insights: (1) the adsorption of the Fe-phen molecules is more energetically favoured through S atoms, rather than PLs, (2) the adsorption of the Fe-phen molecule is not spin dependent, in the sense that there no configurations favourable to only a certain spin state, (3) the adsorption mainly occurs with the Fe atom on top of a Cu from the substrate, (4) the energy difference between the possible configurations it is shown does not allow the transition from one configuration to another even at room temperature.

Insights into the structure of CuN/Cu(100) substrate were made, showing that the

N atoms have a slighty higher height than the Cu atoms. No buckling or oscilating N heights are observed.

The adsorption on the CuN/Cu(100) surface was studied through scanning both vertically and in configurational space. The main conclusion is that the S-based adsorption mechanism relies on close proximity of S atoms to Cu atoms. As in the case of adsorption on the Cu(100) surface, the adsorption is not spin-dependent. We have studied the most energetically favoured configurations (from the results provided by the energy scans) and found that Config.no.1 is one of the most stable of them. The adsorption properties show that the coordination sphere of the Fe atom is very similar to that of the isolated (gas-phase) molecule. The adsorption properties (i.e. the STM images) confirm that the studied geometries are very close to experimental ones.

In the case of Lu-bisphthalocyanine, we may conclude that the Lu atom has no relevant influence over the bond length and valence angles when comparing the $LuPc_2$ with the simple Pc molecule. Another important aspect to be mentioned is the fact that both Pc macrocycles bend to the same degree, confirming the hypothesis that the unpaired electron of the neutral system is delocalized over the whole molecule [49] and sustaining the experimental X-ray diffraction experiments [38].

There are no significant differences between the geometries of the neutral and anion molecular complexes. Both in the case of bond lengths, bond angles and dihedrals, $LuPc_2$ and $[LuPc_2]^-$ are comparable, the most significant difference arising only regarding the interplanar Pc-Pc distance.

Last, but not least, we also observed a decrease in the doming when using the B97-1 functional, as for regular DFT calculations. Moreover the Pc-Pc distance is closer to experimental values, leading us to the conclusion that the C-pots method gives better results for this type of molecular complexes.

In the matter of the IR and Raman spectra, the $LuPc_2$ bands generally reproduce the ones computed for the Phthalocyanine (Pc) molecule, substantial differences being observed only in what concerns the band intensities. As such, we may first of all conclude that there are no important vibrations that involve the Lutetium atom, and second of all, we may say that the increase in intensity is due to the fact that the molecular complex contains two phthalocyanine rings. The vibrations giving rise to bands in the IR and Raman spectra are vibrations in the phthalocyanine rings. We also observe more intense bands in the IR spectrum of the $LuPc_2$ anion.

Selected References

1. G. Binnig, H. Rohrer, C. Gerber, E. Wihel, Phys. Rev. Lett., **50**, 120 (1983).
2. Alexandre Reily Rocha, *Theoretical and computational aspects of electronic transport at the nanoscale*. PhD thesis (University of Dublin, Trinity College, 2007).
3. A.R. Rocha, V.M. García-Suárez, S.W. Bailey, C.J. Lambert, J. Ferrer, S. Sanvito, Nature Materials **4**, 335 (2005).
4. Iijima S., Nature, **354**, 56, (1991).
5. D. Bogdan, R. Isai, A. Calborean and C. Morari, Physica E, **44**, 1441, (2012).
6. R.S. Wagner, W.C. Ellis, Appl. Phys. Lett., **4**, 89, (1964).
7. D.F. Perepichka, F. Rosei, Small, **2**, 22, (2006).
8. J. Bai, X.C. Zeng, H. Tanaka, J.Y. Zeng, P.Natl.Acad.Sci.USA, **101**, 2664, (2004).
9. P. Ordejón, E. Artacho, J.M. Soler, Phys. Rev. B, **53**, R10441, (1996).
10. J.M. Soler, E. Artacho, J.D. Gale, *et al.*, J.Phys.:Condens.Matter,**14**, 2745, (2002).
11. N. Troullier, J.L. Martins, Phys. Rev. B, **46**, 1754, (1992).
12. J.P. Perdew, K. Burke, M. Ernzerhof, Phys. Rev. Lett., **77**, 3865, (1996).
13. M.J. Frisch, G.W. Trucks, H.B. Schlegel, *et.al*, *Gaussian 09, Revision A.02*, Gaussian, Inc., Wallingford CT, 2009.
14. H. Peelaers, B. Partoens, F.M. Peeters, Nano Lett., **9**, 107, (2009).
15. J.K. Böhlke, J.R. de Laeter, P. De Bievre, *et al.*, J. Phys. Chem. Ref. Data, **34**, 57, (2005).
16. P. Gütlich, Y. Garcia, H.A. Goodwin, Chem. Soc. Rev., **29**, 419, (2000).
17. D.F. Shriver, P.W. Atkins, C.H. Langford, *Inorganic Chemistry*, 2nd ed.; Oxford University Press, Oxford, Melbourne, Tokyo, (1994).
18. T. Miyamachi, M. Gruber, V. Davesne, *et al.*, Nat. Commun., **3**, 938, (2012).
19. T.G. Gopakumar, F. Matino, H. Naggert, *et al.*, Angew. Chem. Int. Ed., **51**, 6262, (2012).
20. A.D. Becke, J. Chem. Phys., **98**, 5648, (1993). C. Lee, W. Yang, R.G. Parr, Phys. Rev. B, **37**, 785, (1988). S.H. Vosko, L. Wilk, M. Nusair, Can. J. Phys., **58**, 1200, (1980). P.J. Stephens, F.J. Devlin, C.F. Chabalowski, M.J. Frisch, J. Phys. Chem., **98**, 11623, (1994).
21. A. Schäefer, C. Huber, R. Ahlrichs, J. Chem. Phys., **100**, 5829, (1994).

22. V. Legrand, S. Pillet, H.-P. Weber, *et al.*, J. Appl. Crystallogr., **40**, 1076 (2007). B. Gallois, J.-A. Real, C. Hauw, J. Zarembowitch, Inorg. Chem., **29**, 1152, (1990). M. Marchivie, P. Guionneau, J. Am. Chem. Soc., **124**, 194, (2002).
23. M. Reiher, Inorg. Chem., **41**, 6928, (2002).
24. T. Bučko, J. Hafner, S. Lebèque, J.G. Ángyán, Phys. Chem. Chem. Phys., **14**, 5389, (2012).
25. A. Fouqueau, S. Mer, M.E. Casida, *et al.*, J. Chem. Phys., **120**, 9473, (2004).
26. A. Droghetti, D. Alfé, S. Sanvito, J. Chem. Phys., **137**, 124303, (2012).
27. V. Chiş, A. Droghetti, R. Isai, C. Morari, I. Rungger and S. Sanvito, AIP Conf. Proc., **1565**, 57, (2013).
28. P. Gütlich, Y. Garcia, H. A. Goodwin, Chem. Soc. Rev., **29**, 419, (2000).
29. S. Lebègue, S. Pillet, J.G. Ángyán, Phys. Rev. B, **78**, 024433, (2008).
30. F. Lu, M. Bao, C. Ma, *et al.*, Spectrochim. Acta Part A **59**, 3273 (2003).
31. E. Ortí, J.L. Brédas, C. Clarisse, J. Chem. Phys., **92**, 1228 (1990).
32. I.S. Kirin, P.N. Moskalev, Y.A. Makashev, Russ. J. Inorg. Chem., **10** (1965), 1065.
33. M. Maitrot, G. Guillaud, B. Boudjema, *et al.*, Chem. Phys. Lett., **133** (1987), 59.
34. Y. Açikbaş, M. Evyapan, T. Ceyhan, *et al.*, Sens. Act. B **135**, 426 (2009).
35. I.D. Mackie, G.A.DiLabio, J. Phys. Chem. A, **112**, 10968 (2008).
36. F.A. Hamprecht, A.J. Cohen, D.J. Tozer, N.C. Handy, J. Chem. Phys., **109**, 6264 (1998).
37. S. Grimme, J. Comput. Chem., **27**, 1787 (2006).
38. A. De Cian, M. Moussavi, J. Fischer, R. Weiss, Inorg. Chem., **24**, 3162 (1985).
39. S. Kahlal, A. Mentec, A. Pondaven, M. L'Her, J.-Y. Saillard, New J. Chem., **33**, 574, (2009).
40. I. Bidermane, J. Luder, S. Boudet, *et al.*, J. Chem. Phys., **138**, 234701, (2013).
41. R. Isai, I. Brumboiu, G. Mile, M. Oltean, V. Chiş, in preparation.
42. D.R.T. Zahn, personal communication.
43. W.C. Moreira, R. Aroca, Spectrochim. Acta A, **51** (1995) 2325.
44. J.-J. Andre, K. Holczer, P. Petit, *et al.*, Chem. Phys. Lett., **115**, 463, (1985).
45. R. Murdey, M. Bouvet, M. Sumimoto, *et al.*, Synth. Met., **159**, 1677 (2009).
46. T.R. Cundari, W.J. Stevens, J. Chem. Phys., **98**, 5555 (1993).
47. X. Cao, M. Dolg, J. Chem. Phys., **115**, 7348, (2001). X. Cao, M. Dolg, J. Mol. Struct. (Theochem), **581**, 139, (2002).
48. J. Tersoff, D.R. Hamann, Phys. Rev. B, **31**, 805, (1985).
49. A. Mentec, A. Pondaven, J.M. Kerbaol, M. L'Her, Inorg. Chem. Comm., **9**, 810 (2006).
50. J. Simon, C. R. Chimie, **8**, 893 (2005).